

An Integration Model for Non-isothermal Solidification of Multi-component Alloys in LBM with Ultrasonic Excitation

Yaoqiang Yu ^{1,*}, Tilita George Alexandru ², Wenhao Chen ², Yinsheng Zhong ^{1,2},
Robin Ma ² and Matthew Yuen ^{1,2}

¹ School of Applied Physics and Materials, Wuyi University, Jiangmen, 529020 P. R. Chin

² Hong Kong University of Science and Technology, Hong Kong, China

Corresponding Author: Yaoqiang Yu

ABSTRACT: *Ultrasound is proved to improve microstructure during solidification in Laser Beam Melting (LBM). So, in order to obtain changing of microstructure of different alloys, an integration model is built, consisting of thermal model in Ansys, nucleation model with ultrasonic excitation in MATLAB, and phase field model in MATLAB. The ultrasonic excitation is generated by an acoustic pressure that is a function of frequency and amplification. Due to pressure affected in metal liquid, free energy change on the nucleation selectively changes to be related to chemical potential simultaneously. For optimization of grains-forming simulation, thickness of interface, added noise based on phase field of Fe18Cr8Ni system are conducted. The mean grains size of simulation with 0 frequency are simulated to have a well agreement with experimental result with same frequency. For specific 50k frequency used, the mean grains size is slightly different from experimental results.*

KEYWORDS: *Phase field; Solidification; Non-isothermal condition; Pressure; Multi-component alloys.*

Date of Submission: 03-08-2020

Date of acceptance: 18-08-2020

I. INTRODUCTION

Laser Beam Melting is one of additive manufacture technologies with the advantages that a near-net-shape object can be formed through completely melting powders from layer-by-layer by laser beam. Due to high speed thermal energy transmission from melt zone to the substrate, cooling rate and gradient are sufficiently large that certain mechanical properties are not at the level of conventional manufacturing, which can be seen from a microstructure full of non-equiaxed grains [1-3]. Increasing the number of equiaxed grains is a way to improve mechanical properties. Wang et al [4] used a high-speed camera to record that the bubbles generated by ultrasound can cause damage on the primary arm of dendrites during nucleation, and especially more on the second arm. Other researchers Wang et al [5] found that the cavitation bubbles flow and implode at the interface of Bi-Zn alloy through ultrafast X-ray imaging during solidification. In our group researches [6-8], mechanical properties have been improved by the increasing number of equiaxed grains and ultrasonic excitation plays an important role in achieving that microstructure.

Phase field is a very powerful method to analyze the microstructure evolution of alloys such as steels during solidification in its development. Kobayashi [9] suggested a phase field model for solidification of a pure metal with anisotropy and latent heat due to the formation of various dendrite patterns. Wheeler, Boettinger and McFadden [10] proposed a phase field model (WBM model) for isothermal solidification in binary alloys, which has a limitation on the width of the interface depending on the chemical potential. For eliminating the restriction, Kim et al [11] proposed a model (KKS model) to increase the width of the interface without increasing error rates. Compared to the WBM model, the significant difference is that the KKS model has different concentrations of solid state and liquid state but same chemical potential. Due to the need of many industrial alloys containing at least three components, many researchers extended to the phase field model of multi-component alloys. Cha, Yeon, and Yoon [12] proposed a phase field model applied in isothermal solidification which can perform dendritic patterns of substitutional and interstitial alloys. Kobayashi, Ode, Kim [13] demonstrated a dendritic growth of a model with thermodynamic data calculations to provide a new approach of getting concentration field in time during isothermal solidification. Zhang Ruijie et al [14] developed a more clarified model with diffusion equations for non-isothermal solidification. These phase field models are only to demonstrate the dendritic formation and the morphology growth.

In this work, thermal model is used to get the temperature field as input parameters in the phase field model, the modified KKS phase field model of non-isothermal solidification is to be associated with the periodic pressure that has an influence on the nuclei processing related to free energy. The pressure described later below is

a regular sinusoid. When the liquid solidifies, the nucleation model takes effect, beginning to form. Columnar to equiaxed (CTE) transformation is included to be examined by experimental results. At a certain range of pressure, parts of nucleation are calculated by the control factor, indicating that damaging led by pressure is working. The microstructure then is changed accordingly.

II. METHODOLOGY

2.1. Thermal model

2.1.1. Assumption

This three-dimension transient thermal analysis is based on the following assumptions: Firstly, the fluid flow effect is negligible for the current model. Secondly, the heat transfer of the model only involves the effect of conduction and convection, the effect of radiation is ignored as it accounts for less than 10% of the total heat transfer. Thirdly, laser beam is the only heat source acting on the powder bed. The magnitude of optical penetration depth is several microns for mono-sized powder and it is difficult to estimate the penetration depth precisely. The laser moving source is considered as a Gaussian distributed surface heat flux load input if the finite element size is larger than five grains diameters.

The controlling parameters such as the laser power, laser scan speed and laser beam diameter determine the thermal state of the system for a given set of power and substrate. A macroscale (in the order of 10-3m) FEM thermal model is used to simulate the temperature field as the laser beam is scanning through the powder on top of the substrate. The simulated temperature information in ANSYS will be extracted for the use in the nucleation and grains growth model developed in MATALB.

2.1.2. Governing equations

The temperature distribution across the substrate and deposited material can be determined by solving the three-dimension transient heat conduction equation [15]

$$\rho c \frac{\partial T}{\partial t} = \frac{\partial}{\partial x} \left(k \frac{\partial T}{\partial x} \right) + \frac{\partial}{\partial y} \left(k \frac{\partial T}{\partial y} \right) + \frac{\partial}{\partial z} \left(k \frac{\partial T}{\partial z} \right) + Q \quad (1)$$

where ρ is the material density (kg/m^3); c is the specific heat capacity ($\text{J/kg} \cdot \text{K}$); T is the temperature; t is the interaction time; k is thermal conductivity (W/mK); and $Q(x,y,z,t)$ is the volumetric heat generation (W/m^3). The effective thermal conductivity is a function of porosity of the powder. The porosity of the powder can be calculated as [16]

$$\varphi = \frac{\rho_b - \rho_p}{\rho_b} \quad (2)$$

where φ is the porosity of the powder, ρ_b and ρ_p are the densities of the bulk and powder material. The porosity is assumed to vary from 0.4 for powder state to 0 at solid state [15].

The thermal conductivity of the powder can be expressed as

$$k_p = k_b(1 - \varphi) \quad (3)$$

where k_p and k_b are respectively the thermal conductivities of powder and bulk materials.

The most common beam profile in the laser material processing is the Gaussian distribution of energy shown given by

$$Q_0 = \frac{2AP}{\pi r_0^2} \exp\left(-\frac{2r^2}{r_0^2}\right) \quad (4)$$

Where A is the absorptivity of the powder material which can be calculated if the reflectivity of the material λ is known, as $A = 1 - \lambda$, for a reflectivity of iron; r is the radial distance from the beam center; P is the power of the beam at $r = 0$; and r_0 is radius of the beam, containing 86% of amount of heat [17].

2.1.3. Boundary conditions

There are two boundary conditions applying on the 3D finite element model. The first is defined on the powder bed surface to account for the energy lost due to natural convection.

$$-k \left[\frac{\partial T}{\partial z} \right]_{z=0} = Q - h(T_0 - T_{surf}) \quad (5)$$

where h is the heat transfer coefficient at the powder surface, which is taken as 10 W/mK [15].

The second boundary condition is no energy lost on the bottom surface of the substrate as

$$\left[\frac{\partial T}{\partial Z} \right]_{z=bottom} = 0 \quad (6)$$

The initial condition of uniform temperature distribution throughout the powder bed prior to laser melting at time $t=0$ can be applied as,

$$T(x, y, z, 0) = T_0(x, y, z) \quad (7)$$

where T_0 is the ambient temperature taken as 293 °K.

2.2. Phase field of solidification for multicomponent alloys

2.2.1. Governing equations

The total energy of entire system for multicomponent alloys consisting of free energy and interfacial energy is described as [12]

$$F(\varphi, c_1, \dots, c_{n-1}) = \int_{\Omega} d\Omega [f(\varphi, c_1, \dots, c_{n-1}) + \frac{\varepsilon^2}{2} |\nabla \varphi|^2] \quad (8)$$

where the first term f is free energy density, and C_i is concentration of i^{th} component for a system, φ is a phase parameter ranging from 1 in solid to 0 in liquid, ε is a gradient coefficient related to the interfacial energy σ that is defined in Section 2.1.2.

For the model, the free energy density is defined as [12]

$$f(\varphi, c_1, \dots, c_{n-1}) = h(\varphi) f^S(c_1, \dots, c_{n-1}) + [1 - h(\varphi)] f^L(c_1, \dots, c_{n-1}) + w g(\varphi) \quad (9)$$

where f_S is the free energy density of the solid phase, f_L is the free energy density of the liquid phase, $g(\varphi)$ is a double-well potential, w is its height. And $h(\varphi)$ is an interpolation function of the normalized area under the potential $g(\varphi)$.

The governing equations [12] for phase field and concentration field, respectively, are

$$\frac{1}{M} \frac{\partial \varphi}{\partial t} = - \frac{\delta F}{\delta \varphi} = \nabla \cdot \varepsilon^2 \nabla \varphi - w g'(\varphi) + h'(\varphi) \times [G_d] \quad (10)$$

$$\frac{\partial C_k}{\partial t} = \nabla \cdot \sum_{i=1}^{n-1} \sum_{j=1}^{n-1} M_{ki} f_{c_i c_j} \nabla C_j + \nabla \cdot \sum_{i=1}^{n-1} M_{ki} f_{c_i \varphi} \nabla \varphi \quad (11)$$

where M is mobility of the phase field, G_d is the driving force, M_{ki} is determined from the diffusivity matrix.

$$D_{kj} = \sum_i^{n-1} M_{ki} f_{c_i c_j} \quad (12)$$

2.2.2. Parameters for phase field equations

For the potential $g(\varphi)$ and $h(\varphi)$, their expressions, respectively, are

$$g(\varphi) = \varphi^2 (1 - \varphi)^2 \quad (13)$$

$$h(\varphi) = \varphi^3 (6\varphi^2 - 15\varphi + 10) \quad (14)$$

For taking the parameters ε , w of phase field equation, considering one dimensional solution [12] at equilibrium

$$\varphi_0(x) = \frac{1}{2} \left[1 - \tanh\left(\frac{\sqrt{w}}{\varepsilon \sqrt{2}} x\right) \right] \quad (15)$$

Thus, the relationship of parameters ε , w are obtained as [18]

$$\sigma = \frac{\varepsilon \sqrt{w}}{3\sqrt{2}} \quad (16)$$

$$2\lambda = \alpha \frac{\varepsilon \sqrt{2}}{\sqrt{w}} \quad (17)$$

where α is constant depending on the range of the interface thickness 2λ , e.g., α is 2.2 when ϕ is changing from 0.1 to 0.9, and α is 2.94 when ϕ is from 0.05 to 0.95 [12].

The concentration of any points in the system follows the mixture rule

$$c = h(\varphi) c_s + (1 - h(\varphi)) c_L \quad (18)$$

It can be useful for the interface region. If the region is fully liquid ($\varphi = 0$), then $h(0) = 0$, $c = c_L$, and when the region is fully solid ($\varphi = 1$), then $h(1) = 1$, $c = c_S$. Although the concentration c_S and c_L are not independent of each other, each chemical potential is restricted to be equal [19] at equilibrium.

$$\frac{\partial f_S}{\partial c_S} = \frac{\partial f_L}{\partial c_L} \quad (19)$$

The phase field mobility, M , can be determined using the chemical rate theory that describes interface movement by assuming thermally activated hopping process for individual atoms across the interface [12]. The expression of mobility for the thin interface limit is described as

$$\frac{RT}{VoVm} = \frac{\sigma}{M\varepsilon^2} - \frac{\varepsilon}{\sqrt{2w}} \times \xi(c_1^{L,e}, \dots, c_{n-1}^{L,e}, c_1^{S,e}, \dots, c_{n-1}^{S,e}) \quad (20)$$

where $\xi(c_1^{L,e}, \dots, c_{n-1}^{L,e}, c_1^{S,e}, \dots, c_{n-1}^{S,e})$ is a function derived in [12].

For sharp interface limit $\lambda \rightarrow 0$, Equation (13) can be reduced to

$$\frac{RT}{VoVm} = \frac{\sigma}{M\varepsilon^2} \quad (21)$$

where V_0 is the velocity of interface, set to 1m/s [20] in this work. V_m is the molar volume of a total system.

For a two-dimensional dendritic growth, anisotropic interfacial energy [9] is used as

$$\bar{\varepsilon} = \varepsilon\eta = \varepsilon[1 + \gamma_e \cos(\beta\theta)] \quad (22)$$

where γ_e is the strength of anisotropy, β depends on the morphology of dendritic growth, always taking the value of four as a four-fold symmetry.

Putting Equation 22 in Equation 10, the governing equation for two-dimensional dendritic growth [12] is obtained

$$\frac{1}{M} \frac{\partial \varphi}{\partial t} = \varepsilon\eta\eta'[\sin(2\theta)(\varphi_{yy} - \varphi_{xx}) + 2\cos(2\theta)\varphi_{xy}] - (1/2)\varepsilon^2[\eta^2 - \eta\eta''] [2\sin(2\theta)\varphi_{xy} - \nabla^2\varphi - \cos(2\theta)(\varphi_{yy} - \varphi_{xx})] - w g'(\varphi) + h'(\varphi) \times [G_d] \quad (23)$$

2.2.3. Boundary condition

There are two kinds of boundary conditions applied in the model. Firstly, no-flux conditions are applied to the bottom boundary, which can be expressed as Equation 28. Secondly, periodic condition is applied on the left two and right two ends of the phase field domain, as Equation 29 shown.

$$\varphi(x, H) = \varphi(x, H - 1) \quad (24)$$

$$\varphi(x, H) = \varphi(x - 2, H)$$

$$\varphi(x - 1, H) = \varphi(x - 3, H) \quad (25)$$

2.3. Nucleation model

2.3.1. Normal growth

During solidification, atoms start to gather randomly together, then become a mass region. It is because of the increasing free energy change ΔG as shown in Figure 1. The nucleation forms when ΔG is greater than zeros, and stop to keep on once ΔG turns to be negative. When the radius of nucleation reaches the critical radius of the maximum of ΔG , it can spontaneously grow however ΔG changes, otherwise, it could be possibly dissipated.

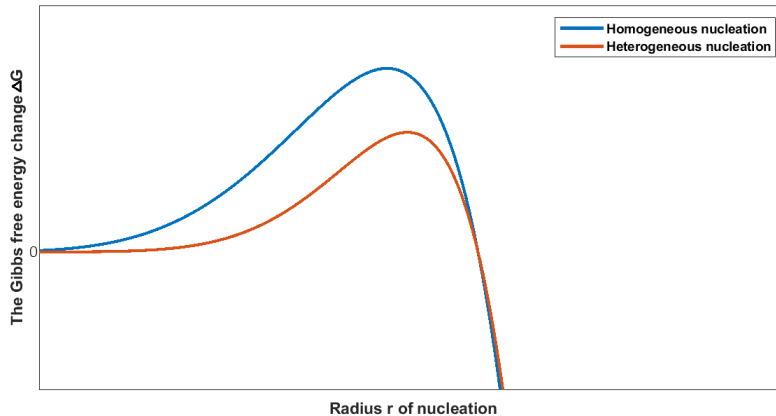


Figure 1. The change of free energy to two types of nucleation

The free energy change follows general relationship, as expressed in Equation 35.

$$\Delta G = \frac{4}{3}\pi r^3 G_d + 4\pi r^2 \sigma \quad (26)$$

The first term is the Gibbs free energy of the volume of nucleation as the difference between the liquid phase and solid phase. The second term is the surface energy due to the interface formed between solid and liquid.

The critical radius can be obtained by the derivation of Gibbs free energy change ΔG to the radius of nucleation in Equation 35.

$$\frac{\partial \Delta G}{\partial r} = 4\pi r^2 G_d + 8\pi r \sigma = 0 \quad (27)$$

Thus, the critical radius of nucleation is

$$r = -\frac{\sigma}{G_d} \quad (28)$$

For the nucleation generated, there are two types of nucleation, the homogeneous and heterogeneous. homogeneous nucleation births in the liquid while heterogeneous nucleation births at an interface between solid and liquid.

Putting the Equation 28 in the Equation 26, the free energy of homogeneous nucleation is obtained

$$G_{\text{hom}} = \frac{16\pi\sigma^3}{3G_d^2} \quad (29)$$

The nucleation rate [21] in time is calculated as

$$N_{\text{hom}} = \int_0^t I_{\text{hom}} dt = \frac{D_i^L}{a^2} \frac{4\pi r_i^2}{a^2} n_L \exp\left(-\frac{G_{\text{hom}}}{k_b T}\right) \exp\left(-\frac{t_{\text{trans}}}{t}\right) t \quad (30)$$

Due to the existed angle for the heterogeneous, the free energy of heterogeneous nucleation is modified as

$$G_{\text{heter}} = \frac{16\pi\sigma^3}{3G_d^2} S(\theta), S(\theta) = \frac{(2 + \cos\theta)(1 - \cos\theta)^2}{4} \quad (31)$$

where $S(\theta)$ is a value from 0 to 1, depending on the shape of nuclei. Thus, heterogeneous nucleation is more likely to occur than homogeneous nucleation, as shown above in Figure 1.

The nucleation rate in time is calculated as

$$N_{\text{heter}} = \int_0^t I_{\text{heter}} dt = \frac{D_i^L}{a^2} \frac{2\pi r_i^2 (1 - \cos\theta)}{a^2} n_L \exp\left(-\frac{G_{\text{heter}}}{k_b T}\right) \exp\left(-\frac{t_{\text{trans}}}{t}\right) t \quad (32)$$

Considering the columnar-to-equiaxed transition for alloys during solidification, the number of nucleation is re-formula as [22]

$$n(\Delta T) = \frac{N_{\text{max}}}{\sqrt{2\pi}\Delta T_\sigma} \int_0^{\Delta T} \exp\left[-\frac{(\Delta T - \Delta T_N)^2}{2(\Delta T_\sigma)^2}\right] d(\Delta T) \quad (33)$$

where ΔT_N is the mean nucleation undercooling, ΔT_σ is the standard deviation of the distribution and N_{max} is the maximum nucleation density.

2.3.2. Ultrasonic excitation on nuclei

The pressure of ultrasound is a function of frequency and amplitude. The expression of its acoustic pressure in liquid is obtained as [23]

$$P_{ac} = 2\pi f_{us} A_{mp} \rho_L C_s \cdot \sin(2\pi f_{us} t) \quad (34)$$

where f_{us} is a frequency, A_{mp} is amplitude of ultrasound, ρ_L is liquid metal density, C_s is speed of sound through material.

The printing layer thickness is always very thin, close to tens of micrometer [24-26] in laser beam melting, so that we assume the hydrostatic pressure without ultrasound is atmosphere pressure. Therefore, when ultrasound works in the liquid, the total pressure of liquid in the system becomes

$$P_{ht} = P_{ac} + P_a \quad (35)$$

The cavitation occurs when P_{ht} is below vaporization pressure P_v , which is 8 Pa for alloys melting . It is because at low pressure there are air pockets trapped into the liquid [23]. The bubbles that their inherent frequency related to

their size should be greater than ultrasonic frequency can stay for micro milliseconds T_{bubble} [27] in liquid along with expanding and contraction. For when bubbles can have implosion and how pressure shockwaves can generate, the remaining time T_{bubble} of any of them from start to end, pressure P_{gas} [28] ,radius r [29]and bubbles' frequency f_{bubble} [30] at any time before explosion, respectively, are should be obtained from

$$T_{bubble} = \frac{1}{4 f_{fus}} \quad (36)$$

$$P_{gas} = (P_a + \frac{2\sigma_{press}}{r}) (\frac{r^3 - (\frac{r}{8.543})^3}{r_{max}^3 - (\frac{r}{8.543})^3})^j \quad (37)$$

$$r = \left(\frac{2h}{t} \right)^2 \frac{3Cs\rho_L}{8g(\rho_L - \rho_b)} \quad (38)$$

$$f_{bubble} = \frac{1}{2\pi r} \sqrt{\frac{3\varphi P_h}{\rho_L}} \quad (39)$$

where j is the recommended value of 1.4.

At a certain time, a bubble implodes at maximum pressure P_{max} [31]. Shockwave from the bubble is permeating the liquid, it has a speed v_b [32]and can generate nucleation by reducing the r_{max} [27] of in the regions that the shockwave can permeate. The expressions are shown below

$$P_{max} = P_{gas} \left(\frac{8.54 \times r_{max}}{r} \right)^{3j} \quad (40)$$

$$v_b = \frac{1}{\rho_L} \sqrt{\frac{P_{max} - P_a}{\rho_L^{-1} - \rho_p^{-1}}} \quad (41)$$

$$r_{max} = \frac{\sqrt{2(P_v + P_{ac} - P_a)T_{bubble}^2}}{3\rho_L} \quad (42)$$

Shockwaves density P_{bubble} [28]and the density of liquid ρ_p [32]at maximum pressure, respectively, are derived from

$$P_{bubble} = B \left[2 \frac{n-1}{n+1} \left(\frac{v_b}{Cs} - 1 \right) + 1 \right]^{\frac{2n}{n-1}} - B, n = 7.15 \quad (43)$$

$$\rho_p = \rho_L^n \sqrt{\frac{P_{max} + B}{P_a + B}} \quad (44)$$

where B is a function of temperature [33], and for simplify calculation, set as

$$B = \frac{\rho_L Cs^2}{n} \quad (45)$$

When nucleation is affected by shockwave, due to the non-isobar system, the free energy change for the condition that nucleation happens in the constant pressure of system is not useful any more. Thus, it changes to [34]

$$G_{press} = \frac{16\pi\sigma_{press}^3 V_C^2}{3[\Delta G_{press} V_C + (V_S - V_C)(P_{bubble} - P_a)]^2} S(\theta), S(\theta) = \frac{(2 + \cos\theta)(1 - \cos\theta)^2}{4} \quad (46)$$

where $S(\theta)$ is an angle for heterogeneous nucleation, and is a value of 1 for the homogeneous, ΔG_{press} is a chemical potential related to the latent heat of fusion [34] , σ_{press} is the interfacial energy for it [35], they are shown below

$$\Delta G_{press} = \frac{\Delta H_f \times (T - T_m)}{T_m} \quad (47)$$

$$\sigma_{press} = 0.49 \times 3 \sqrt[3]{\frac{V_C}{N_a} \frac{\Delta H_f}{V_C}} \quad (48)$$

where N_a is Avergadero constant

The nucleation rate [34] then is derived

$$N_{press} = 10^{40} e^{\left(\frac{-G_{press}}{K_b T}\right)} \quad (49)$$

where K_b is Boltzmann constant, $1.38064852 \times 10^{-23}$.

For easily differentiation between ultrasonically affected and unaffected nucleation, and decreasing the cost of time to run program, the nucleation is reformed by introducing a step function as a control factor to control nucleation condition

$$N = n(\Delta T)[1 - u(f_{bubble} - f_{us})u(P_v - P_{ht})u(r_{max} - r_0)u(0.5 - \phi)] + \quad (50)$$

$$10^{40} e^{\left(\frac{-G_{press}}{K_b T}\right)} [u(f_{bubble} - f_{us})u(P_v - P_{ht})u(r_{max} - r_0)u(0.5 - \phi)], f_{bubble} > f_{us}, P_v > P_{ht}, r_{max} > r_0, 0.5 > \phi$$

2.4. Calculation of Phase Diagrams (CALPHAD) method and temperature field

The CALPHAD method is very useful for obtaining thermodynamic equilibrium information for multicomponent systems [26]

$$G = G^o + G^{ideal} + G^{excess} + G^{mag} \quad (51)$$

where the first term G^o is the Gibbs free energy for pure components in the system, G^{ideal} is the molar Gibbs free energy for ideal solution, G^{excess} is the molar excess Gibbs energy describing the deviation from ideal solution, G^{mag} is the contribution due to magnetic ordering. Their forms, respectively, are

$$G^o = \sum_{i=1}^n x_i G_i^o \quad (52)$$

$$G^{ideal} = RT \sum_i^n c_i \ln c_i \quad (53)$$

$$G^{excess} = \sum_{i=1}^m \sum_{j=m+1}^n x_i x_j L_{i,j} + \sum_{i=1}^m \sum_{j=m+1}^k \sum_{y=k+1}^n x_i x_j x_y L_{i,j,z} + \dots + \sum_{i=1}^m \sum_{j=m+1}^k \dots \sum_{z=x+1}^n x_i x_j \dots x_z L_{i,j,\dots,z} \quad (54)$$

$$G^{mag} = RT \ln(\beta + 1) f(\tau), \tau = T / T_c \quad (55)$$

The solid free energy G_s and liquid free energy G_L , respectively, can be obtained from Equation 30 .So that driving force G_d which pushes phase transition becomes

$$G_d = f_s - f_L + \sum_{i=1}^n (c_i^L - c_i^S) f_{c_i^L}^L \quad (56)$$

where $f_s, f_L, f_{c_i^L}^L$ are $G_s / V_m, G_L / V_m, \partial f_L / \partial C_i^L$.

The temperature field for the whole system is obtained by

$$T = T_0 + T_{gradient} \times h \times dx - T_{coolingrate} \times dt \quad (57)$$

where T_0 is initial temperature, h is cross-sectional length, dx is a grid length, $T_{cooling}$ is cooling rate, $T_{gradient}$ is temperature gradient, dt is a time step.

III. PARAMETERS OF GRAINS SIMULATION FOR OPTIMIZATION

In order to validate that the simulation result is well in agreement with experimental results, mean grains size is accounted for comparison. Here Fe18Cr8Ni steel is selected to be tested, the thermal model properties of it are shown as Table 1. The enthalpy and thermal conductivity are illustrated in [15]. The point C is picked out to get thermal field as described in Figure 2.

Parameter	Value
Laser beam power	175 W
Laser beam spot	0.1 mm
Scanning speed	1 cm/s
Powder layer size (length)x(width)x(depth)	6 mm x 4 mm x 0.3 mm
Powder layer mesh	0.04 mm
Substrate size (length)x(width)x(depth)	50 mm x 50 mm x 60 mm
Substrate size	5 mm

Table 1. Thermal model properties

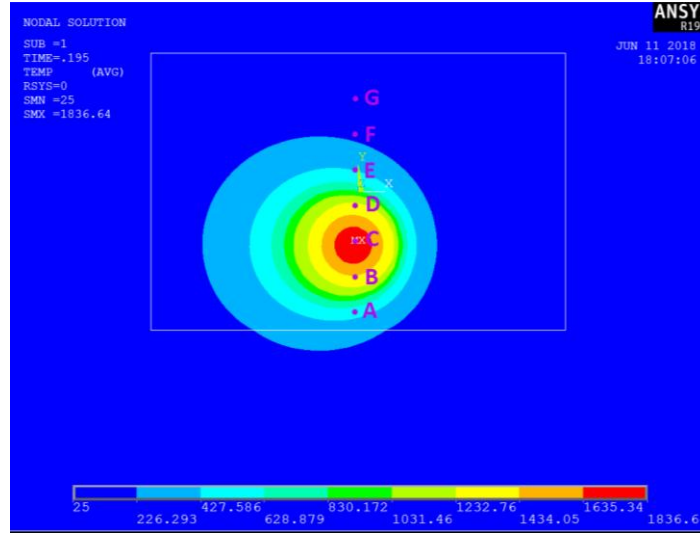


Figure 2. The powder heated condition by laser beam

The thermodynamic descriptions of Fe18Cr8Ni system can be evaluated as [26]

$$\begin{aligned}
 G_L = & RT[FeL \times \log(FeL) + CrL \times \log(CrL) + NiL \times \log(NiL)] + FeL \times \\
 & [132659 + 117576T - 235143T \log(T) - 439752 \times 10^{-3} T^2 \\
 & - 589269 \times 10^{-8} T^3 + 773585/T - 367516 \times 10^{-21} T^7] + NiL \times [112356 + 108457 \times T \\
 & - 22096 \times T \times \log(T) - 48407 \times 10^{-3} \times T^2 - 382318 \times 10^{-21} \times T^7] \\
 & + CrL \times [154830 + 146060 \times T - 26908 \times T \times \log(T) + \\
 & 189435 \times 10^{-3} \times T^2 - 147721 \times 10^{-6} \times T^3 + 139250/T + 237615 \times 10^{-21} \times T^7] + \\
 & (13022 \times FeL + 13177 \times CrL + 3133 \times NiL) \times NiL \times FeL \times CrL + \\
 & FeL \times NiL \times [-16911 + 5162 \times T + (10180 - 4147 \times T) \times (FeL - NiL)] + \\
 & CrL \times FeL \times [-17737 + 7997 \times T + 1331 \times (FeL - CrL)] + \\
 & CrL \times NiL \times [318 - 7332 \times T + (16941 - 637 \times T) \times (CrL - NiL)];
 \end{aligned}
 \tag{58}$$

$$\begin{aligned}
 G_s = & RT[FeS \times \log(FeS) + CrS \times \log(CrS) + NiS \times \log(NiS)] + \\
 & FeS \times [-236.7 + 132.416T - 24.6643T \log(T) - \\
 & 3.75752 \times 10^{-3} T^2 - 5.89269 \times 10^{-8} T^3 + 77359/T] + \\
 & NiS[-5179.159 + 117.854T - 22.096T \log(T) - 4.8407 \times 10^{-3} T^2] + \\
 & CrS[-1572.94 + 157.643T - 26.908T \log(T) + 1.89435 \times 10^{-3} T^2 - 1.47721 \times 10^{-6} T^3 \\
 & + 139250/T] + FeS \times RT \log(0.7 + 1) \left[-\left(\frac{(T/67)^{-5}}{10} + \frac{(T/67)^{-15}}{315} + \frac{(T/67)^{-25}}{1500} \right) / 2015306 \right] + \\
 & NiS \times RT \log(0.52 + 1) \left[-\left(\frac{(T/633)^{-5}}{10} + \frac{(T/633)^{-15}}{315} + \frac{(T/633)^{-25}}{1500} \right) / 2015306 \right] + \\
 & CrS \times RT \log(0.82 + 1) \left[-\left(\frac{(T/367)^{-5}}{10} + \frac{(T/367)^{-15}}{315} + \frac{(T/367)^{-25}}{1500} \right) / 2015306 \right] + \\
 & 1618 \times NiS \times FeS \times CrS + FeS \times NiS \times [-12054 + 3274T + \\
 & (11082 - 445T)(FeS - NiS) - 726 \times (FeS - NiS)^2] + \\
 & CrS \times FeS \times [10833 - 7477T - 1410(FeS - CrS)] + \\
 & CrS \times NiS \times [8030 - 1288T + (33080 - 16036T)(CrS - NiS)];
 \end{aligned} \tag{59}$$

The other specific parameters of phase field model are listed in Table 2.

Parameter	Value
Diffusion Cr in liquid[36]	$2.51 \times 10^{-7} \times e^{\left(\frac{-66900}{RT}\right)}$ m2/s
Diffusion Cr in solid	$7.7 \times 10^{-6} \times e^{\left(\frac{-251000}{RT}\right)}$ m2/s
Diffusion Ni in liquid	$1.35 \times 10^{-6} \times e^{\left(\frac{-89200}{RT}\right)}$ m2/s
Diffusion Ni in solid	$2 \times 10^{-5} \times e^{\left(\frac{-272000}{RT}\right)}$ m2/s
Entropy	8.2304T J/K
Volume	$6.8298 + 5.19 \times 10^{-4} T$ m3/mol
Interfacial energy for phase field equations [37]	$\frac{7.0781T}{\sqrt[3]{6.02 \times 10^{23} \times (6.8298 + 5.19 \times 10^{-4} T)^2}}$ J/m2
Cr in weight	18 %
Ni in weight	8 %
Temperature gradient	1.25×10^{-6} k/m
Cooling rate	10^{-4} k/s
Density of solid metal	8050 kg/m3
Density of liquid metal	7600 kg/m3
Heat of fusion[38]	285 J/g
Melting Temperature	1673 K
Atmosphere pressure	101325 Pa
Speed of sound Cs	5790 m/s
θ of heterogeneous nucleation after explosion of bubbles	$150^\circ C$
θ of heterogeneous nucleation without explosion of bubbles	$30^\circ C$
Anisotropy γ_e	0.04
dt	1^{-8} s
dx	1^{-7} m
Height for simulation	300
Length for simulation	180

Table 2. Other parameters

3.1 Thickness of interface between liquid and solid

Thickness of the interface, 2λ , is always defined by a value in many literature papers. For precision of grains simulation, set the thickness of interface as dx , $3dx$, $5dx$, $7dx$, $9dx$, and $11dx$, respectively. Obviously, mean grains size increases along with increasing thickness of interface shown in Figure 3. This is because thickness of interface 2λ is inversely proportional to the height of the double well potential, w , but is directly proportional to the gradient of the interfacial energy, ε . Putting Equation 16 into Equation 17, we can obtain the two relationships below

$$2\lambda = \alpha \frac{6}{\omega} \sigma \quad (60)$$

$$2\lambda = \alpha \frac{\varepsilon^2}{3\sigma} \quad (61)$$

where interfacial energy, σ , as a function of temperature and alloy composition [39] and constant, α , are independent of w and ε .

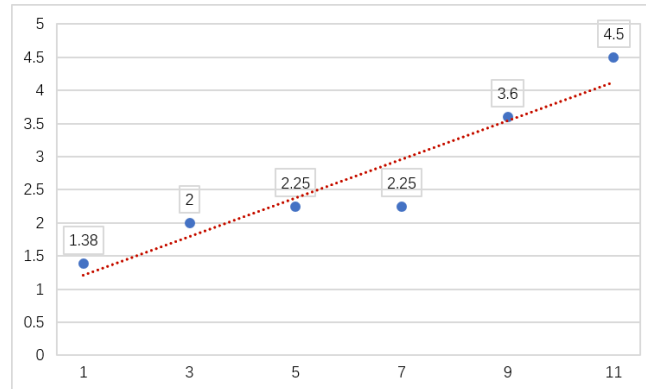


Figure3. Increasing grains size with increasing thickness

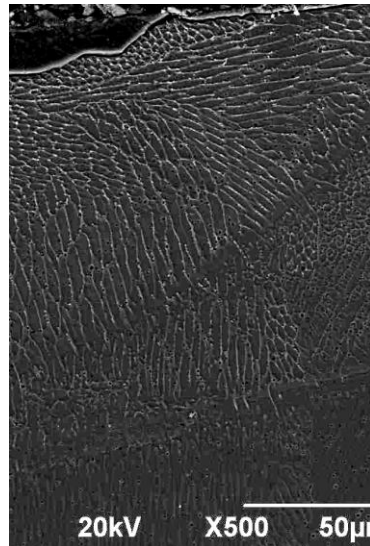


Figure 4. Cross-sectional microstructure of Fe18Cr8Ni steel without ultrasonic excitation

Therefore, increasing thickness 2λ can lead to dropping height of potential w and the gradient coefficient increasing, then affecting free energy of the system in Equation 2. When the right term in Equation 3 is increasing, the size of the grains is increasing as well. Because the experimental mean grains size shown in Figure 4 is $3.6 \mu\text{m}$, here, $9dx$ is chosen as a recommended value.

3.2 Noise added to phase field

Random noise is used to add into dendritic growth in order to increase the instability of crystal forming cross-section. It is because cross-section microstructure also has some irregular formation of grains [40-42]. With random noise, the calculated microstructure seems to generate other different morphologies to compared

with the experimental grains. So, set the various value of amplitude of noise at 0.1, 0.3, 0.5, 0.7 and 0.9, their grains growths are shown in Figure 5. The expression is obtained by

$$\varphi = \varphi \times (1 + \xi_{Noise} \times R_{random}) \quad (62)$$

Where φ is phase field, ξ_{Noise} is noise coefficient, R_{random} is random position which noise can add into a selected position in whole phase field.

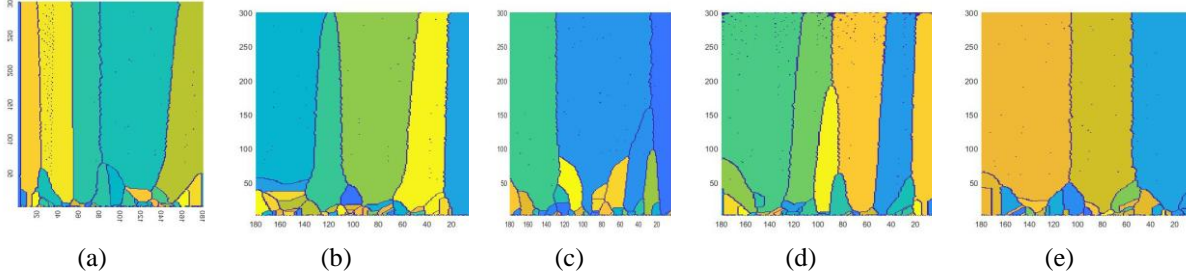


Figure 5. Grains field at noise value of (a) 0.1, (b) 0.3, (c) 0.5, (d) 0.7, (e) 0.9

As have described in 3.1 section, 9dx of thickness is chosen, so the ideal mean grains size is 3.6 μm . Interestingly, their mean grains sizes don't keep constant, which are shown in Figure 6. The mean grains sizes of noise 0.5 and noise 0.9 are 6 μm . The reason for that is mainly great instability of grains growth which can cause the mean grains size to be increased, which is not allowed to have a high influence on mean grains size. For calculations, 0.1 or 0.3 noise is also recommended. Here, 0.3 is chosen as the noise value.

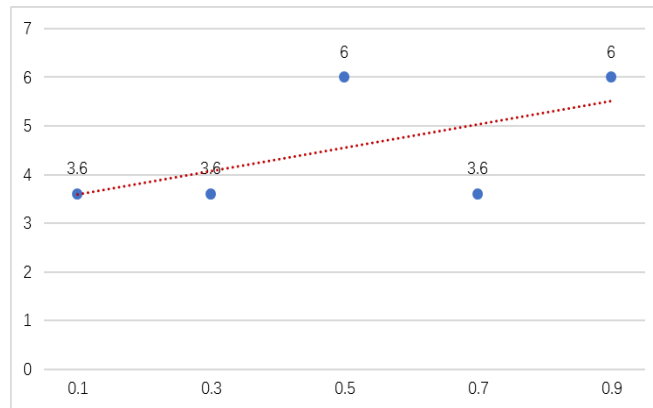


Figure 6. Increasing grains size with increasing thickness

IV. Application to Fe18Cr8Ni steel with ultrasonic excitation

4.1 Interface of program

The nucleation model and phase field model are programmed into codes in MATLAB, and packaged as an app shown in Figure 7. The input parameters should be typed to run. The GUI interface can reflect the acoustic pressure immediately for further research of ultrasound excitation as the frequency and amplitude are inputted. If parameters of 50,000 Hz, 0.5 μm are inputted, then acoustic pressure will instantly change to corresponding values as depicted in Figure 8. The red sine curve is an acoustic pressure, and the yellow line is a vapor pressure which helps to figure out when nucleation is greatly influenced under ultrasonic excitation. If the value of frequency or amplitude is 0, the pressure becomes a static and steady state as shown in Figure 9. When all input parameters are inputted completely, the model can start to calculate. As a consequence, the microstructure is obtained as shown before in Figure 3.

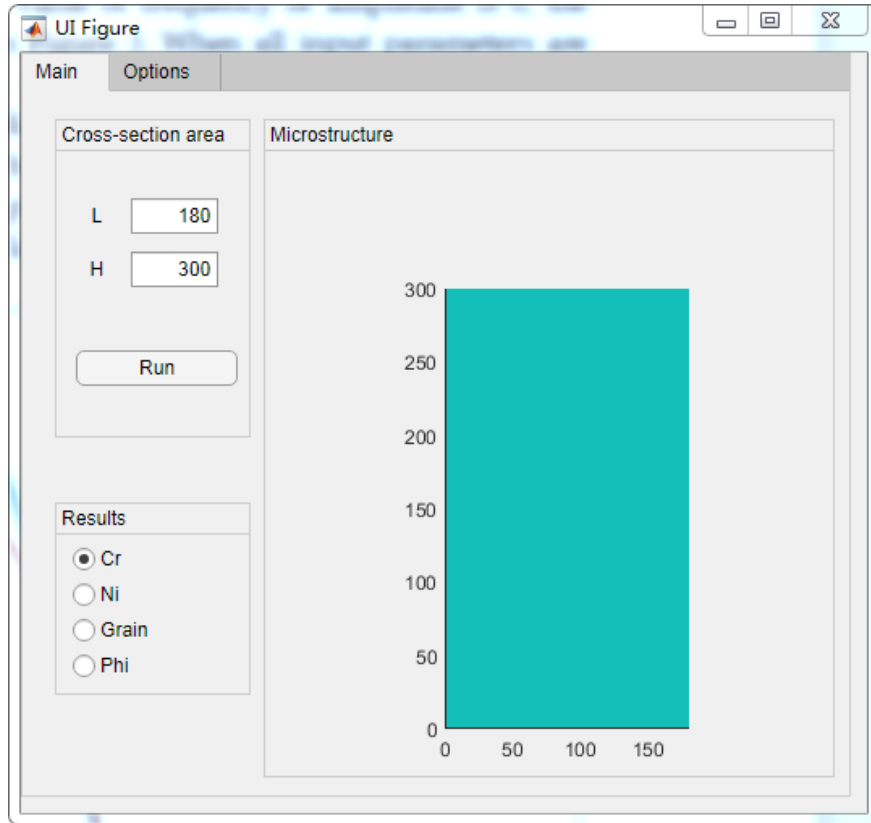


Figure 7. The interface of app

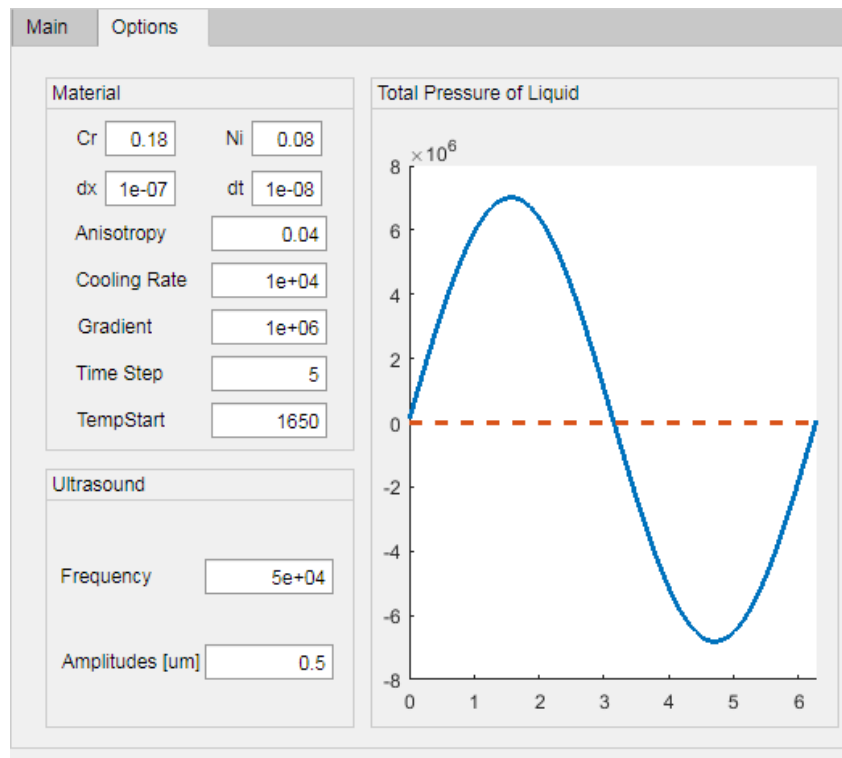


Figure 8. The Total pressure of liquid

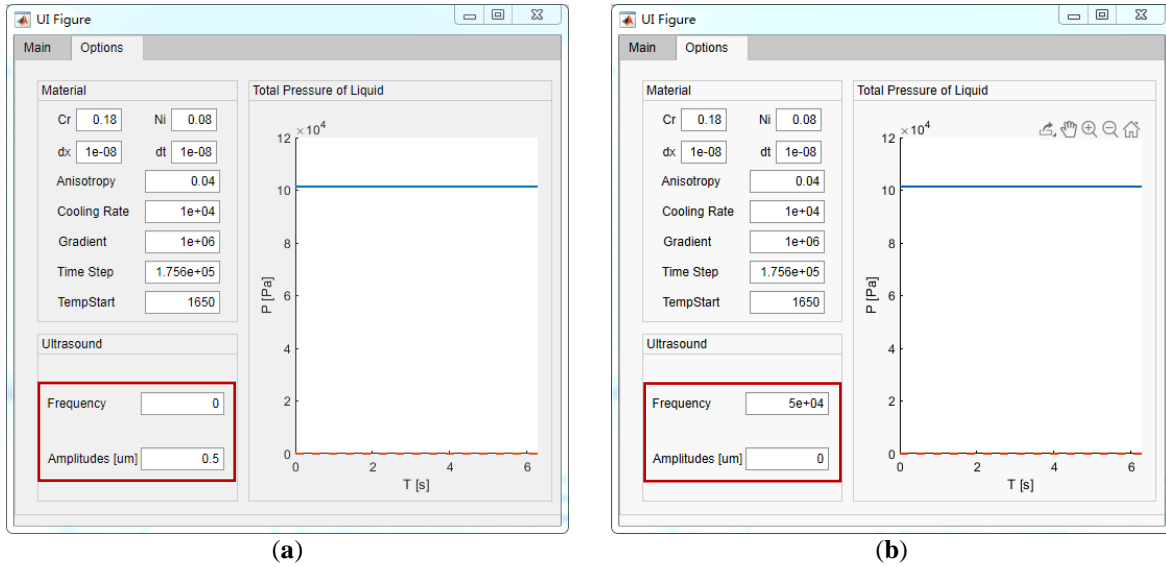


Figure 9. Total pressure in metal liquid (a) with frequency of 0 Hz, (b) with amplitudes of 0 m

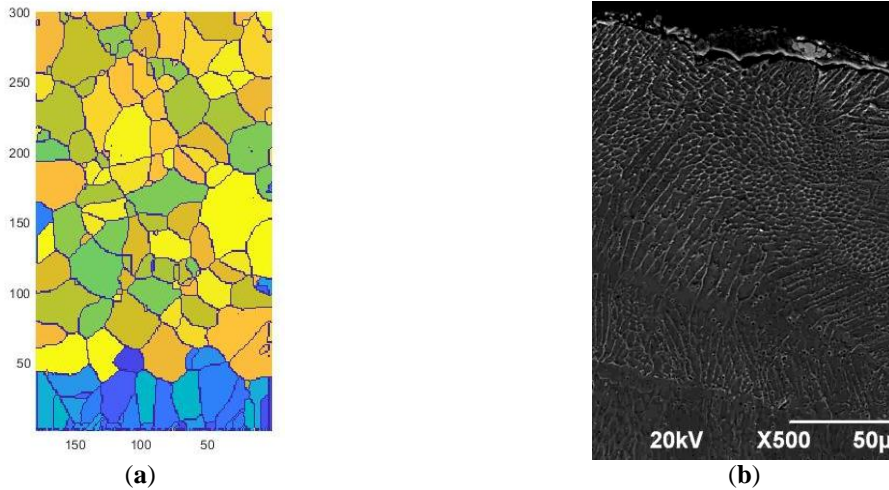


Figure 10. Microstructure with ultrasonic excitation (a) of simulation, (b) of experimental cross-section

4.2 Grains field after ultrasonic excitation

In order to verify the reliability of microstructure with ultrasonic excitation, we made use of the printer with ultrasonic excitation from the Hong Kong University of Science and Technology to print components that have been illustrated previously in [8]. Its printing parameters are mainly 50,000 Hz frequency, 5×10^{-7} m amplitude, 100 W power, 0.6 mm laser spot, and 1.4 m/min scanning speed, respectively. The simulation and cross-section microstructure are shown in Figure 10. It is obvious that the simulation has more homogeneous grains and less columnar grains. This is because some nuclei have been satisfied ultrasonic condition at a range of time when acoustic pressure is below vapor pressure, following ultrasonic nucleation calculation to generate later equiaxed grains. Therefore, the number of columnar grains can also be decreased.

V. DISCUSSION

We firstly optimized grains field of simulation with 0 frequency of ultrasonic excitation which is a normal dendritic growth. By adjusting the variables of thickness and noise, the mean grains size is very close to experimental mean grains size. However, under the given ultrasonic excitation with 50,000 Hz frequency, the mean grains size is 2.25 μm whereas the experimental mean grains size is 3.71 μm . The ratio of simulated average grains size to experimental is 0.61. The difference between them is caused because grains growth with ultrasonic excitation affects the total mean grains size. The precision of ultrasonic nucleation needs further calibration. Due to complex cavitation movement and complicated implosion mechanism, the specific parameters of ultrasonic nucleation for grains growth need much work as well.

VI. CONCLUSIONS

The integration model has a simulation from printing to microstructure. The printing parameters, such as laser beam spot, scanning speed, laser power, can generate relative thermal field. Different thermal field can lead to various microstructure in phase field model. It is better way to observe how microstructure changes under simulated material instead of metallographic or SEM observation of experiment on cross-sectional surface area. However, the precision on thermal model in ANSYS is only up to the order of 10^{-3} m. The model needs a professional performance of a computer. Thus, the values of thermal field are relatively rough when input into the microstructure simulation with an order of 10^{-7} m. Meanwhile, the ultrasonic nucleation should be modified to match experimental result, which can be expressed by the mean grains size and ratio between simulation and experiment. In addition, both the angle on ultrasonic nucleation and on normal nucleation here are fixed. It is because the automagical angle calculation are difficult to be handled during heterogeneous nucleation process. Therefore, it needs to be fixed with various value for all kinds of alloys.

Author Contributions: Yaoqiang Yu: Data curation, Formal analysis, Software, Writing – original draft, Writing – review & editing. Tilita George Alexandru: Conceptualization, Formal analysis, Investigation, Methodology, Project administration, Resources, Software, Validation, Supervision, Writing – review & editing. Wenhao Chen: Data curation, Formal analysis, Investigation, Methodology, Project administration, Resources, Software. Yinsheng Zhong: Supervision, Writing – review & editing. Robin Ma: Supervision. Matthew Yuen: Project administration, Supervision, Writing – review & editing.

Funding: The project was funded by Wuyi University Research Fund and research grants ITF/321/15 and ITF/464/17FP from Hong Kong Innovation and Technology Commission.

Acknowledgments: This work is supported by Wuyi University and Hong Kong University of Science and Technology's 3d printing technology. The author would like to acknowledge the help of colleagues of Hong Kong University of Science and technology.

Conflicts of Interest: The authors declare no conflict of interest.

REFERENCES

- [1]. Y.J. Liu, Z. Liu, Y. Jiang, G.W. Wang, Y. Yang, L.C. Zhang, Gradient in microstructure and mechanical property of selective laser melted AlSi10Mg, *Journal of Alloys and Compounds*, Volume 735, 2018, Pages 1414-1421, ISSN 0925-8388, <https://doi.org/10.1016/j.jallcom.2017.11.020>.
- [2]. Wei Xiong, Liang Hao, Yan Li, Danna Tang, Qian Cui, Zuying Feng, Chunze Yan, Effect of selective laser melting parameters on morphology, microstructure, densification and mechanical properties of supersaturated silver alloy, *Materials & Design*, Volume 170, 2019, 107697, ISSN 0264-1275, <https://doi.org/10.1016/j.matdes.2019.107697>.
- [3]. Maria L. Montero-Sistiaga, Miguel Godino-Martinez, Kurt Boschmans, Jean-Pierre Kruth, Jan Van Humbeeck, Kim Vanmeensel, Microstructure evolution of 316L produced by HP-SLM (high power selective laser melting), *Additive Manufacturing*, Volume 23, 2018, Pages 402-410, ISSN 2214-8604, <https://doi.org/10.1016/j.addma.2018.08.028>.
- [4]. S. Wang, J. Kang, X. Zhang, Z. Guo, Dendrites fragmentation induced by oscillating cavitation bubbles in ultrasound field, *Ultrasonics*, Volume 83, 2018, Pages 26-32, ISSN 0041-624X, <https://doi.org/10.1016/j.ultras.2017.08.004>.
- [5]. Bing Wang, Dongyue Tan, Tung Lik Lee, Jia Chuan Khong, Feng Wang, Dmitry Eskin, Thomas Connolley, Kamel Fezzaa, Jiawei Mi, Ultrafast synchrotron X-ray imaging studies of microstructure fragmentation in solidification under ultrasound, *Acta Materialia*, Volume 144, 2018, Pages 505-515, ISSN 1359-6454, <https://doi.org/10.1016/j.actamat.2017.10.067>.
- [6]. Tilita, G.A.; Chen, W.; Kwan, C.C.F.; Yuen, M.M.F., The effect of ultrasonic excitation on the microstructure of selective laser melted 304 L stainless steel. *Mat.wiss. u. Werkstofftech.* Volume 48, 2017a, Pages 342–348. ISSN 0933-5137, <https://doi.org/10.1002/mawe.201600763>.
- [7]. George-Alexandru Tilita, Wenhao Chen, Cassandra K.L. Leung, Charles C.F. Kwan, Robin L.W. Ma, Matthew M.F. Yuen, Influence of ultrasonic excitation on the mechanical characteristics of SLM 304L stainless steel, *Procedia Engineering*, Volume 216, 2017, Pages 18-27, ISSN 1877-7058, <https://doi.org/10.1016/j.proeng.2018.02.084>.
- [8]. George-Alexandru Tilita, Wenhao Chen, Robin Ma, Charles C.F. Kwan, Matthew Yuen, Effect of ultrasonic excitation on the process of L-PBFAM, *Journal of Materials Processing Technology*, Volume 277, 2020, 116436, ISSN 0924-0136, <https://doi.org/10.1016/j.jmatprotec.2019.116436>.
- [9]. Ryo Kobayashi. Modeling and numerical simulations of dendritic crystal growth. *Physica D: Nonlinear Phenomena*. Volume 63, Issues 3–4, 1993, Pages 410-423, ISSN 0167-2789, [https://doi.org/10.1016/0167-2789\(93\)90120-P](https://doi.org/10.1016/0167-2789(93)90120-P).
- [10]. Wheeler, AA; Boettinger, WJ; McFadden, GB. Phase-field model for isothermal phase transitions in binary alloys. *Physical review. A, Atomic, Molecular, and Optical Physics*. Volume 45, Issue 10, 1992, ISSN 7424-7439, <https://doi.org/10.1103/PhysRevA.45.7424>.
- [11]. Kim, SG; Kim, WT; Suzuki, T. Phase-field model for binary alloys. *Phys Rev E Stat Phys Plasmas Fluids Relat Interdiscip Topics*. Volume 60, Issue 6, 1999, ISSN 1186-7197, <https://doi.org/10.1103/PhysRevE.60.7186>.
- [12]. P.-R, Cha; D.-H, Yeon; J.-K, Yoon. A phase field model for isothermal solidification of multicomponent alloys. *Acta Materialia*, Volume 49, Issue 16, 2001, Pages 3295-3307, ISSN 1359-6454, [https://doi.org/10.1016/S1359-6454\(01\)00184-7](https://doi.org/10.1016/S1359-6454(01)00184-7).
- [13]. Hiroki, Kobayashi; Machiko, Ode; Seong, Gyoony; Kim, Won; Tae, Kim; Toshio, Suzuki. Phase-field model for solidification of ternary alloys coupled with thermodynamic database. *Scripta Materialia*, Volume 48, Issue 6, 2003, Pages 689-694, ISSN 1359-6462, [https://doi.org/10.1016/S1359-6462\(02\)00557-2](https://doi.org/10.1016/S1359-6462(02)00557-2).
- [14]. Ruijie, Zhang; Tao, Jing; Wanqi, Jie; Baicheng, Liu. Phase-field simulation of solidification in multicomponent alloys coupled with thermodynamic and diffusion mobility databases. *Acta Materialia*, Volume 54, Issue 8, 2006, Pages 2235-2239, ISSN 1359-6454, <https://doi.org/10.1016/j.actamat.2006.01.029>.
- [15]. Ahmed Hussein, Liang Hao, Chunze Yan, Richard Everson, Finite element simulation of the temperature and stress fields in single layers built without-support in selective laser melting, *Materials & Design (1980-2015)*, Volume 52, 2013, Pages 638-647, ISSN 0261-3069, <https://doi.org/10.1016/j.matdes.2013.05.070>.

- [16]. Bian, P.; Shao, X.; Du, J. Finite Element Analysis of Thermal Stress and Thermal Deformation in Typical Part during SLM. *Appl. Sci.* 2019, 9(11), 2231, <https://doi.org/10.3390/app9112231>.
- [17]. Lars-Erik Lindgren, 5 - Nonlinear heat flow, Editor(s): Lars-Erik Lindgren, In *Woodhead Publishing Series in Welding and Other Joining Technologies, Computational Welding Mechanics*, Woodhead Publishing, 2007, Pages 47-53, ISBN 9781845692216, <https://doi.org/10.1533/9781845693558.47>.
- [18]. Yeon, Dong-Hee & Cha, Pil-Ryung & Yoon, Jong-Kyu, A phase field study for ferrite–austenite transitions under paraequilibrium. *Scripta Materialia - SCRIPTA MATER*, Volume 45, 2001, Page 661-668, [https://doi.org/10.1016/S1359-6462\(01\)01077-6](https://doi.org/10.1016/S1359-6462(01)01077-6).
- [19]. Kitashima, Tomonori. Coupling of the phase-field and CALPHAD methods for predicting multicomponent. solid-state phase transformations. *Philosophical Magazine - PHILOS MAG.* 88:11, 2008, 1615-1637, <https://doi.org/10.1080/14786430802243857>.
- [20]. P.-R. Cha; D.-H. Yeon; J.-K. Yoon. Phase-field model for multicomponent alloy solidification. *J. Cryst. Growth*, Volume 274, 2005, Pages 281–293, <https://doi.org/10.1103/PhysRevE.71.041609>.
- [21]. D. Stefanescu, *Science and Engineering of Casting Solidification*. Springer, 2015.
- [22]. T. Volkman; D. M. Herlach; W. Löser. Nucleation and phase selection in undercooled Fe-Cr-Ni melts: Part I. Theoretical analysis of nucleation behavior. *Metall. Mater. Trans. A*, Volume, 28, 1997, Page 453–460. <https://doi.org/10.1007/s11661-997-0146-y>.
- [23]. N. Marinescu, *Machining Technologies with Beams and Oscillations*. 1st ed. Bucharest: Bren Publishing House, 2003.
- [24]. Agius, D.; Kourousis, K.I.; Wallbrink, C. A Review of the As-Built SLM Ti-6Al-4V Mechanical Properties towards Achieving Fatigue Resistant Designs. *Metals* 2018, Volume 8, <https://doi.org/10.3390/met8010075>.
- [25]. Chao Wei; Lin Li; Xiaoji Zhang; Yuan-Hui Chueh. 3D printing of multiple metallic materials via modified selective laser melting. *CIRP Annals*, Volume 67, Issue 1, 2018, Pages 245-248, ISSN 0007-8506, <https://doi.org/10.1016/j.cirp.2018.04.096>.
- [26]. Xuezhí, Shi; Shuyuan, Ma; Changmeng, Liu; Qianru, Wu. Parameter optimization for Ti-47Al-2Cr-2Nb in selective laser melting based on geometric characteristics of single scan tracks. *Optics & Laser Technology*, Volume 90, 2017, Pages 71-79, ISSN 0030-3992, <https://doi.org/10.1016/j.optlastec.2016.11.002>.
- [27]. C. Virone; H. Kramer; G. van, Rosmalen. A. Stoop and T. Bakker, Primary nucleation induced by ultrasonic cavitation. *Journal of Crystal Growth*, Volume 294, 2006, Pages 9-15, <https://doi.org/10.1016/j.jcrysgro.2006.05.025>.
- [28]. Y. MATSUMOTO; M. AOKI. Growth and Collapse of Cavitation Bubbles: Distribution Change of Cavitation Nuclei due to the Collapse of Cavitation Bubbles. *Bulletin of JSME*, Volume 27, Issue 229, 1984, Pages 1352-1357, <https://doi.org/10.1299/jsme1958.27.1352>.
- [29]. S. Ridah. Shock waves in water. *Journal of Applied Physics*, Volume 64, 1988, Pages 152-158, <https://doi.org/10.1063/1.341448>.
- [30]. V. Baidakov; K. Bobrov. Spontaneous cavitation in a Lennard-Jones liquid at negative pressures. *The Journal of Chemical Physics*, Volume 140, 2014, Pages 184-506, <https://doi.org/10.1063/1.4874644>.
- [31]. K. Vokurka. Comparison of Rayleigh's, Herring's, and Gilmore's models of gas bubbles. *Acta Acustica united with Acustica*, vol. 59, 1986.
- [32]. J. Holzfuss; M. Rüggeberg; A. Billo. Shock Wave Emissions of a Sonoluminescing Bubble. *Physical Review Letters*, Volume 81, 1998, Pages 5434-5437, <https://doi.org/10.1103/PhysRevLett.81.5434>.
- [33]. S. Ridah. Shock waves in water, *Journal of Applied Physics*. Volume 64, 1988, Pages 152-158, <https://doi.org/10.1063/1.341448>.
- [34]. C. Virone; H. Kramer; G. van, Rosmalen; A. Stoop; T. Bakker. Primary nucleation induced by ultrasonic cavitation. *Journal of Crystal Growth*, Volume 294, 2006, Page 9-15, <https://doi.org/10.1016/j.jcrysgro.2006.05.025>.
- [35]. Bernard Vinet, Lena Magnusson, Hasse Fredriksson, Pierre Jean Desré, Correlations between Surface and Interface Energies with Respect to Crystal Nucleation, *Journal of Colloid and Interface Science*, Volume 255, Issue 2, 2002, Pages 363-374, ISSN 0021-9797, <https://doi.org/10.1006/jcis.2002.8627>.
- [36]. Josef Tomiska, The system Fe–Ni–Cr: revision of the thermodynamic description, *Journal of Alloys and Compounds*, Volume 379, Issues 1–2, 2004, Pages 176-187, ISSN 0925-8388, <https://doi.org/10.1016/j.jallcom.2004.02.027>.
- [37]. J. Miettinen. Thermodynamic-kinetic simulation of constrained dendrite growth in steels. *Metall. Mater. Trans. B*, Volume 31, Issues 2, 2000, Pages 365–379, <https://doi.org/10.1007/s11663-000-0055-6>.
- [38]. T. Koseki; M. C. Flemings. Solidification of undercooled Fe-Cr-Ni alloys: Part I. Thermal behavior. *Metall. Mater. Trans. A*, Volume 26, Issues 11, 1995, Pages 2991–2999, <https://doi.org/10.1007/BF02669655>.
- [39]. Volkman, T., Herlach, D.M. & Löser, W. Nucleation and phase selection in undercooled Fe-Cr-Ni melts: Part I. Theoretical analysis of nucleation behavior. *Metall and Mat Trans A*, Volume 28, 1997, Pages 453–460, <https://doi.org/10.1007/s11661-997-0146-y>.
- [40]. Junwen Zhao, Chao Xu, Guangze Dai, Shusen Wu, Jing Han, Microstructure and properties of rheo-diecasting wrought aluminum alloy with Sc additions, *Materials Letters*, Volume 173, 2016, Pages 22-25, ISSN 0167-577X, <https://doi.org/10.1016/j.matlet.2016.02.143>.
- [41]. Lin-Zhi Wang, Wen-Hou Wei. Selective Laser Melting of 30CrMnSiA Steel: Laser Energy Density Dependence of Microstructural and Mechanical Properties. *Acta Metallurgica Sinica*, Volume 31, 2018, Pages 807-814, <https://doi.org/10.1007/s40195-018-0717-5>.
- [42]. Yan, M., & Yu, P. An Overview of Densification, Microstructure and Mechanical Property of Additively Manufactured Ti-6Al-4V — Comparison among Selective Laser Melting, Electron Beam Melting, Laser Metal Deposition and Selective Laser Sintering, and with Conventional Powder. 2015, <http://dx.doi.org/10.5772/59275>.